
Widespread longitudinal snow dunes in Antarctica shaped by sintering

In the format provided by the authors and unedited

Contents

Supplementary Figures	2
Supplementary Notes	15
Supplementary Text	18

List of Figures

Figure S1	3
Figure S2	4
Figure S3	5
Figure S4	6
Figure S5	7
Figure S6	8
Figure S7	9
Figure S8	10
Figure S9	11
Figure S10	11
Figure S11	12
Figure S12	13
Figure S13	14
Figure S14	16
Figure S15	17

List of Tables

Table S1	5
----------	---

Supplementary Figures

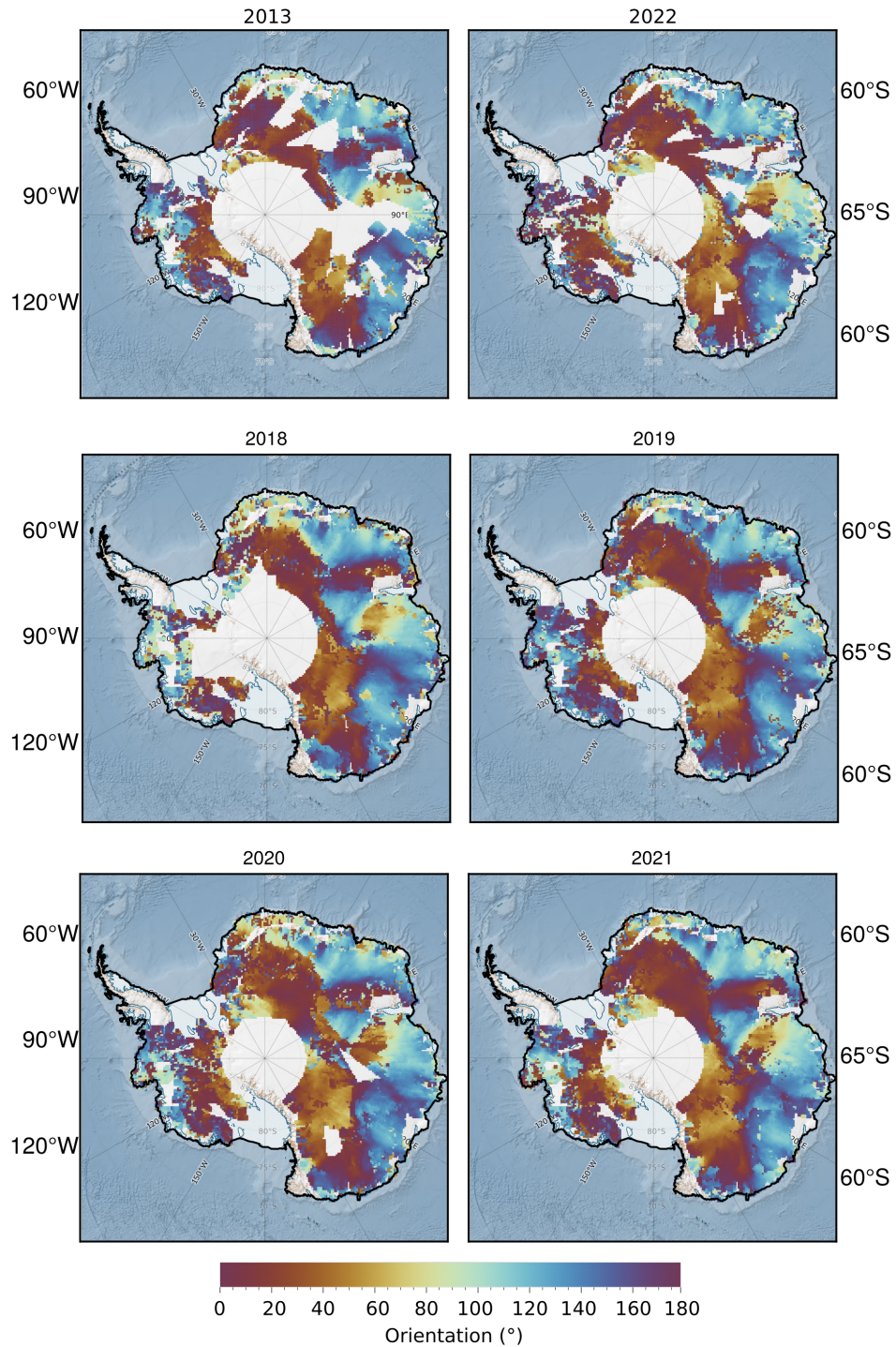


Figure 1: Maps of dune orientation for 6 years. Dune orientation was retrieved at $25 \text{ km} \times 25 \text{ km}$ resolution from satellite imagery between November and December for 2013, January and February 2022 and for November and December for each year between 2018 to 2021.

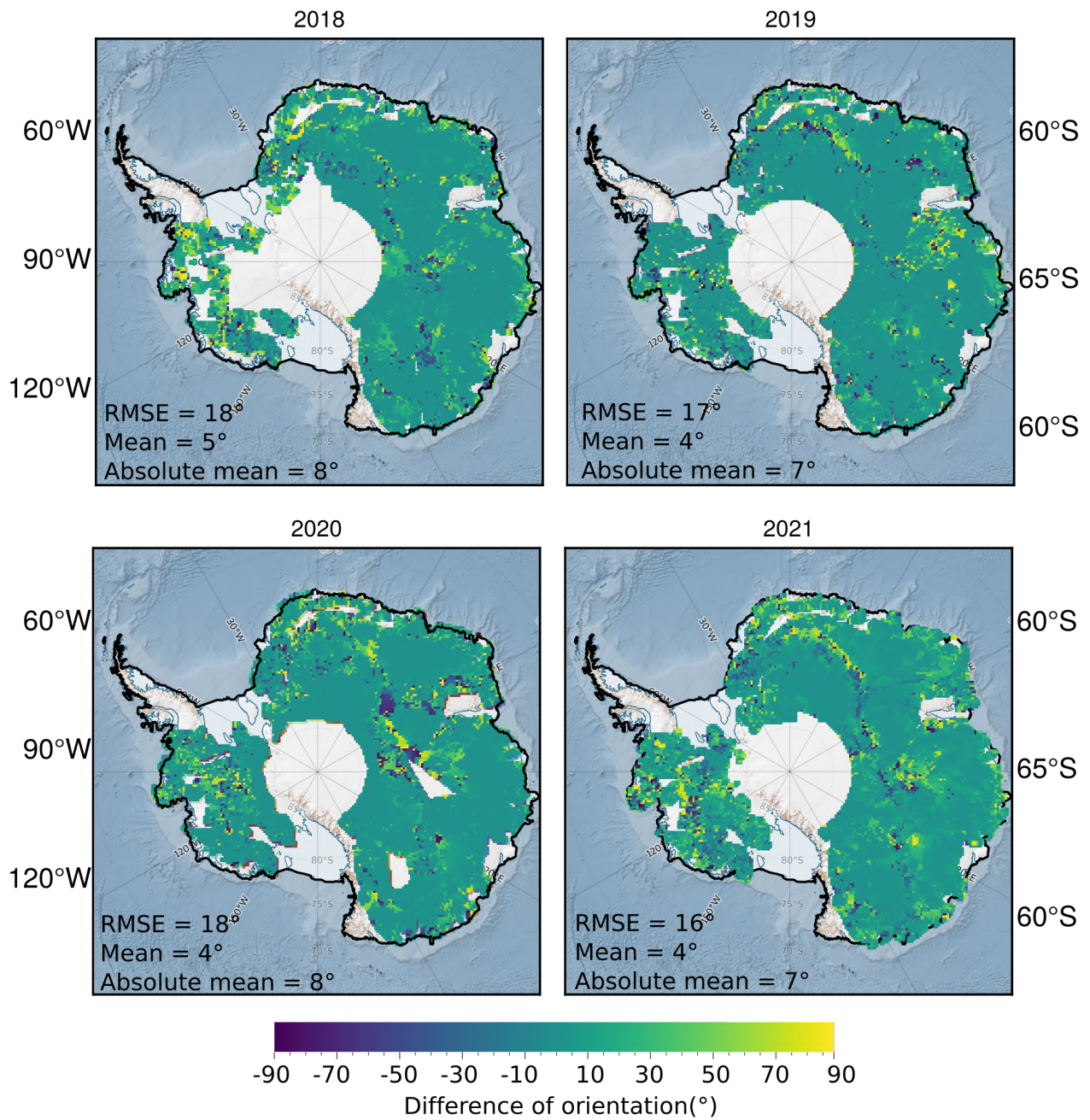


Figure 2: Maps of orientation differences between the mean state analyzed in the main text (over 2018–2021) and in November and December of each year (2018–2021) at 25 km x 25 km resolution.

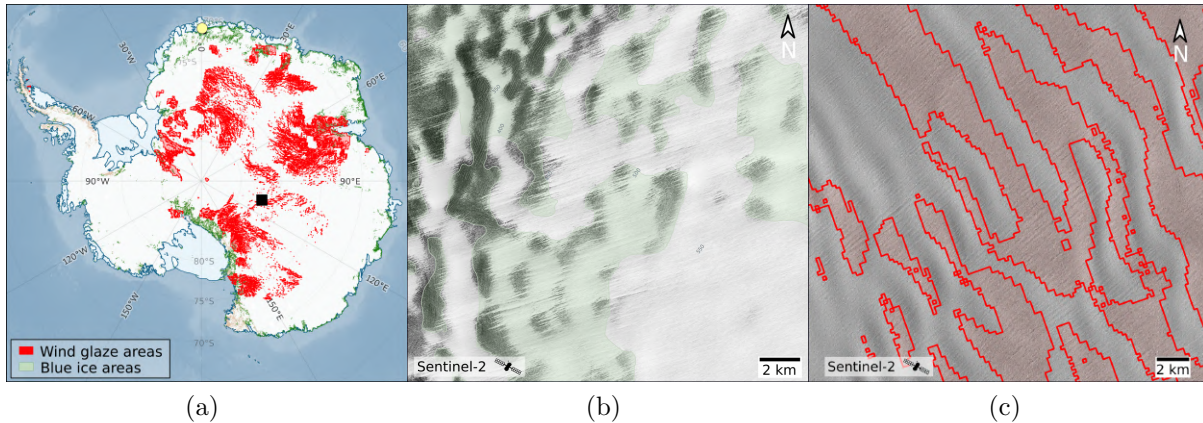


Figure 3: (a) Map of blue ice areas (BIA, in green) and wind glaze areas (red). Linear dunes are detected over 97% of the wind glaze areas. (b) Example of a Sentinel-2 (NIR channel) image (71.53°S , 0.51°E , the yellow dot circled in black in map (a)) with BIA, dunes are partially present over this BIA. (c) Example of a Sentinel-2 image (81.65°S , 109.2°E , the black square in map (a)) over a wind glaze area (red shaded areas), dunes are present all over this area, unless its extent along wind direction is too large ($\sim \geq$ km) [1].

Mode	Type of dunes		
	Longitudinal	Oblique	Transverse
Bed-instability	3	43	54
Elongating	89	11	0
None	18	77	5

Table 1: Contingency table relating the type of dunes to the formation modes. The values are percentage of observations.

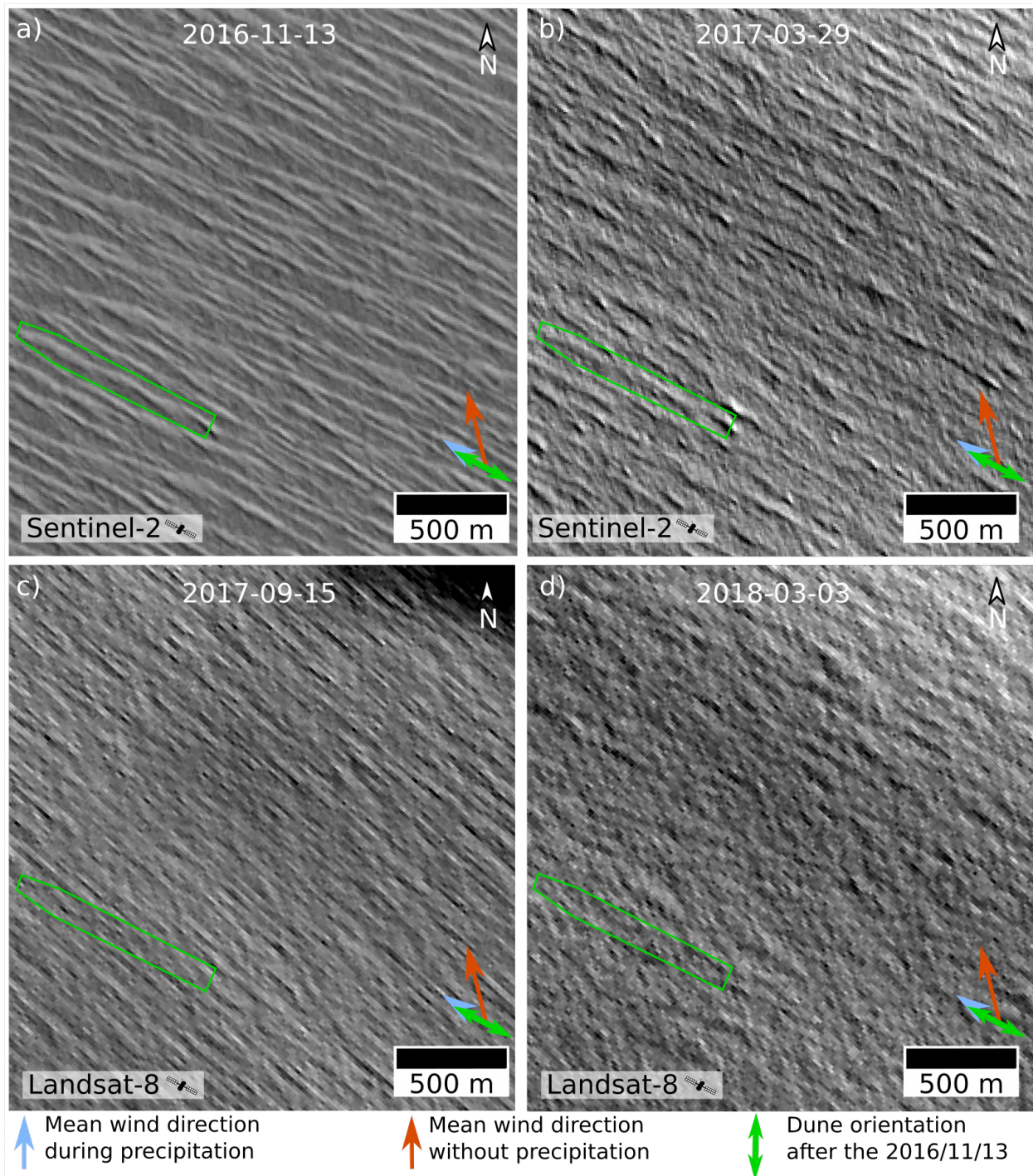


Figure 4: Timeseries of satellite images (NIR channel for Sentinel-2 images and PAN channel for Landsat-8 images) (67.2°S , 138.5°E , close to the area in Fig S8). The dunes seen on 2016-11-13 (a) are still present on 2017-03-29 (b) and partially on 2017-09-15 (c). It is not visible anymore on 2018-03-03 (d). The blue arrows represent the mean wind direction during precipitation. Red arrows represent the mean wind direction without precipitation. The green rectangle delineate a dune, for the sake of visualization.

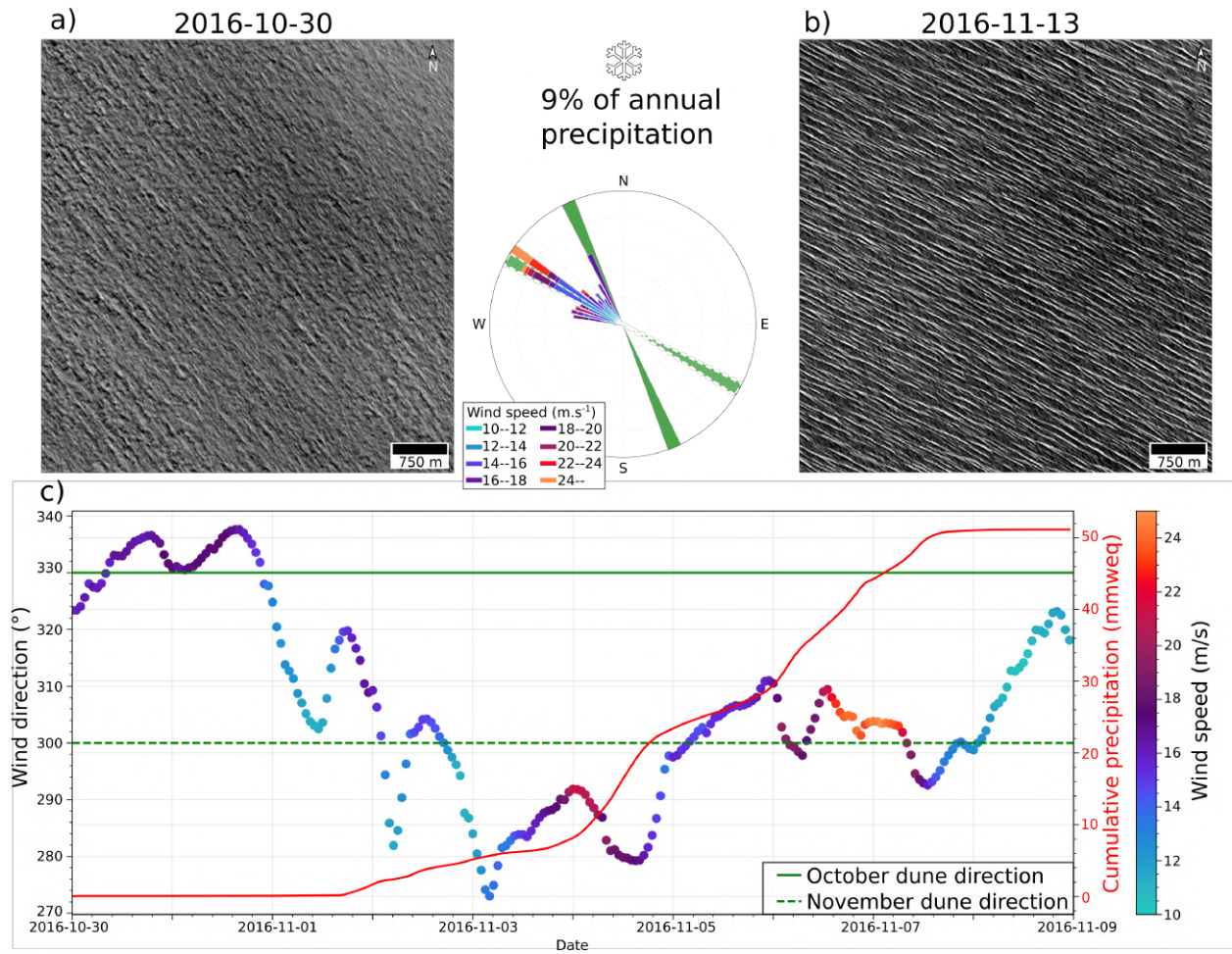


Figure 5: Satellite images (Sentinel-2, NIR channel) around 67.3°S, 138.5°E before (a) and after (b) a precipitation event in spring 2016. (c) Cumulative precipitation and wind speed and direction from the ERA-5 reanalysis. This event corresponds to an atmospheric river according to criteria from [2]. Such kind of re-orientation event was also observed on sea ice in October 2012 [3].

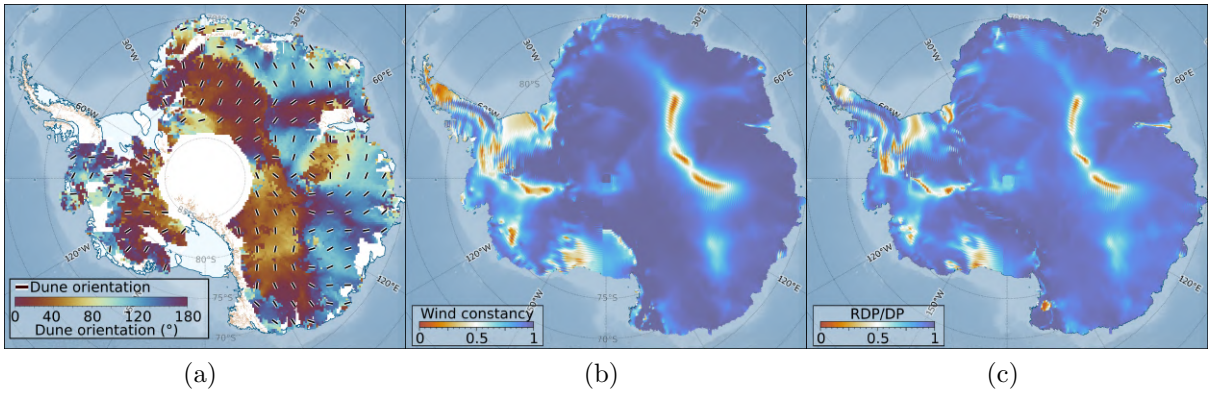


Figure 6: (a) Map of the mean dune orientation at $25 \text{ km} \times 25 \text{ km}$ resolution retrieved from satellite imagery between November and December 2018–2021. (b) Wind constancy derived from the ERA-5 wind speed and direction between 2018 and 2021. The constancy is the ratio of $\sum_{t=2018}^{2021} \|u(\vec{t})\|$ over $\|\sum_{t=2018}^{2021} u(\vec{t})\|$ with $u(\vec{t})$ the wind vector at the time t . It characterizes the directional variability of wind. When the ratio $\rightarrow 1$ the wind tends to be unidirectional whereas when $\rightarrow 0$ it is multidirectional. (c) Snow flux constancy (RDP/DP) calculated from the ERA-5 wind speed and direction between 2018 and 2021. It is the ratio of the resultant drift potential (the norm of the mean snow flux vector) over the drift potential (the mean of the norms of the snow flux vectors).

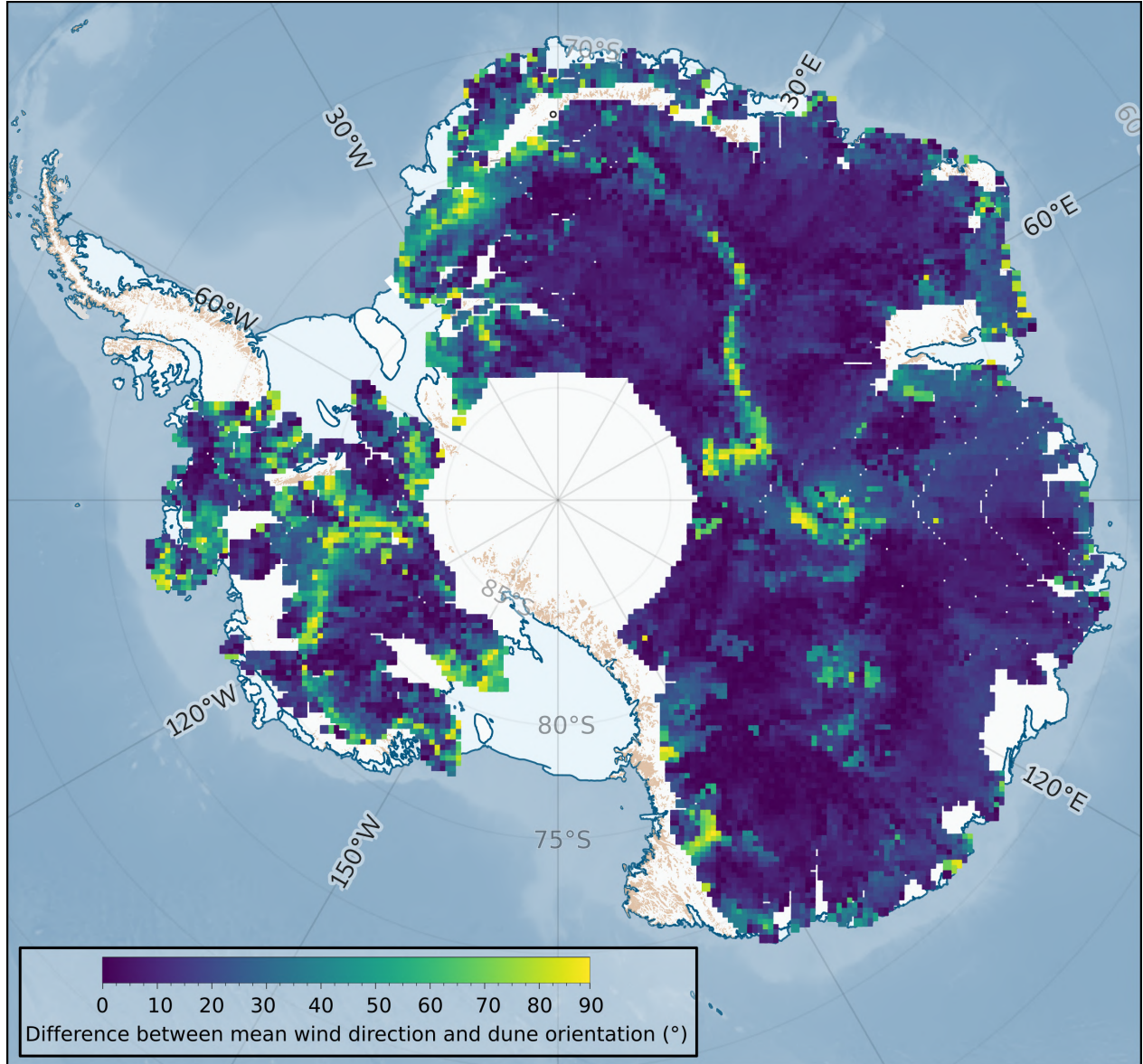


Figure 7: Map of the differences between wind direction and dune orientation. Dune orientation is from November and December 2018–2021 and is resampled at the wind data resolution ($0.25^\circ \times 0.25^\circ$).

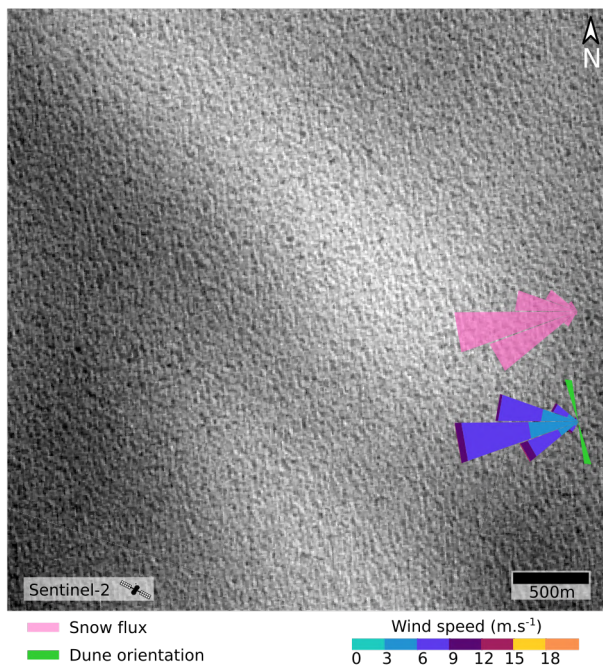


Figure 8: Satellite image (Sentinel-2, NIR channel) of transverse dunes ($73.47563388^{\circ}\text{S}$, $69.89749465^{\circ}\text{E}$). The wind roses show the annual wind regime and snow flux from the ERA-5 Reanalysis.

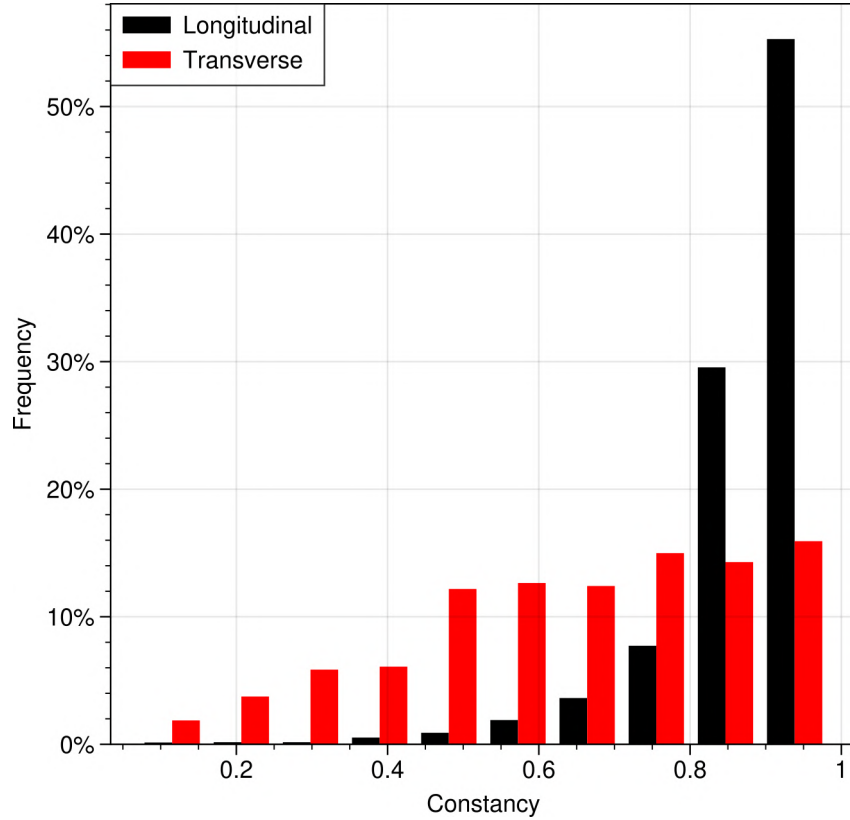


Figure 9: Histogram of the wind directional constancy between 2018 and 2021 for the longitudinal and transverse dunes in Antarctica.

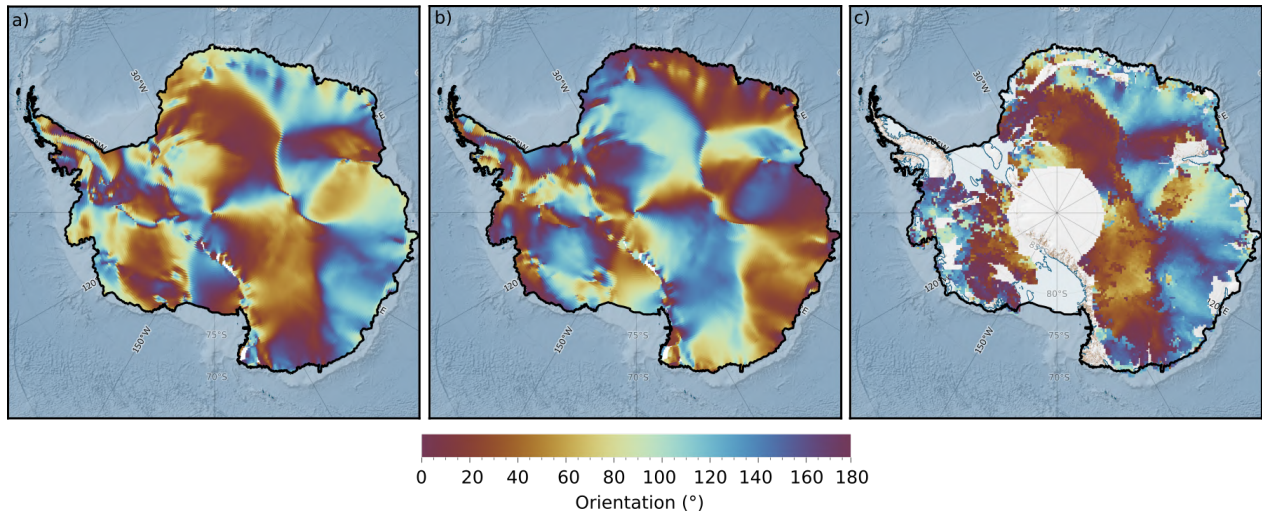


Figure 10: Dune direction calculated using sand dune theory [4] and the snow flux formulation proposed by [5]. To select periods with probable snow transport, only 10-m wind speeds over 6 m s^{-1} are used. (a) Elongating mode orientation. (b) Bed-instability mode orientation. For the sake of comparison, the bed-instability mode orientation is plotted between 0° and 180° . (c) Observed dune orientation by satellite.

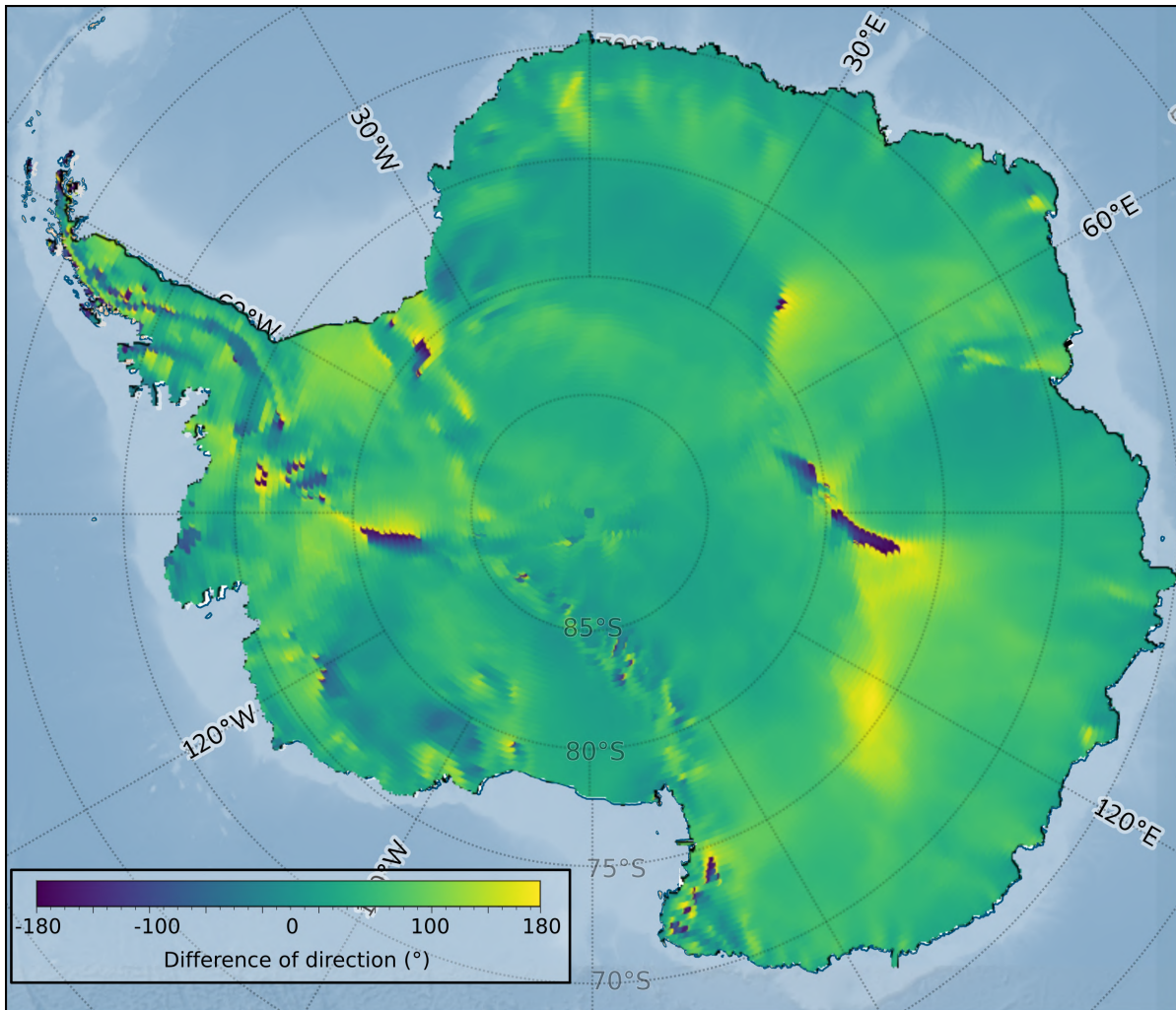


Figure 11: Difference between wind direction during precipitation and wind direction without precipitation, averaged over the period 2018–2021.

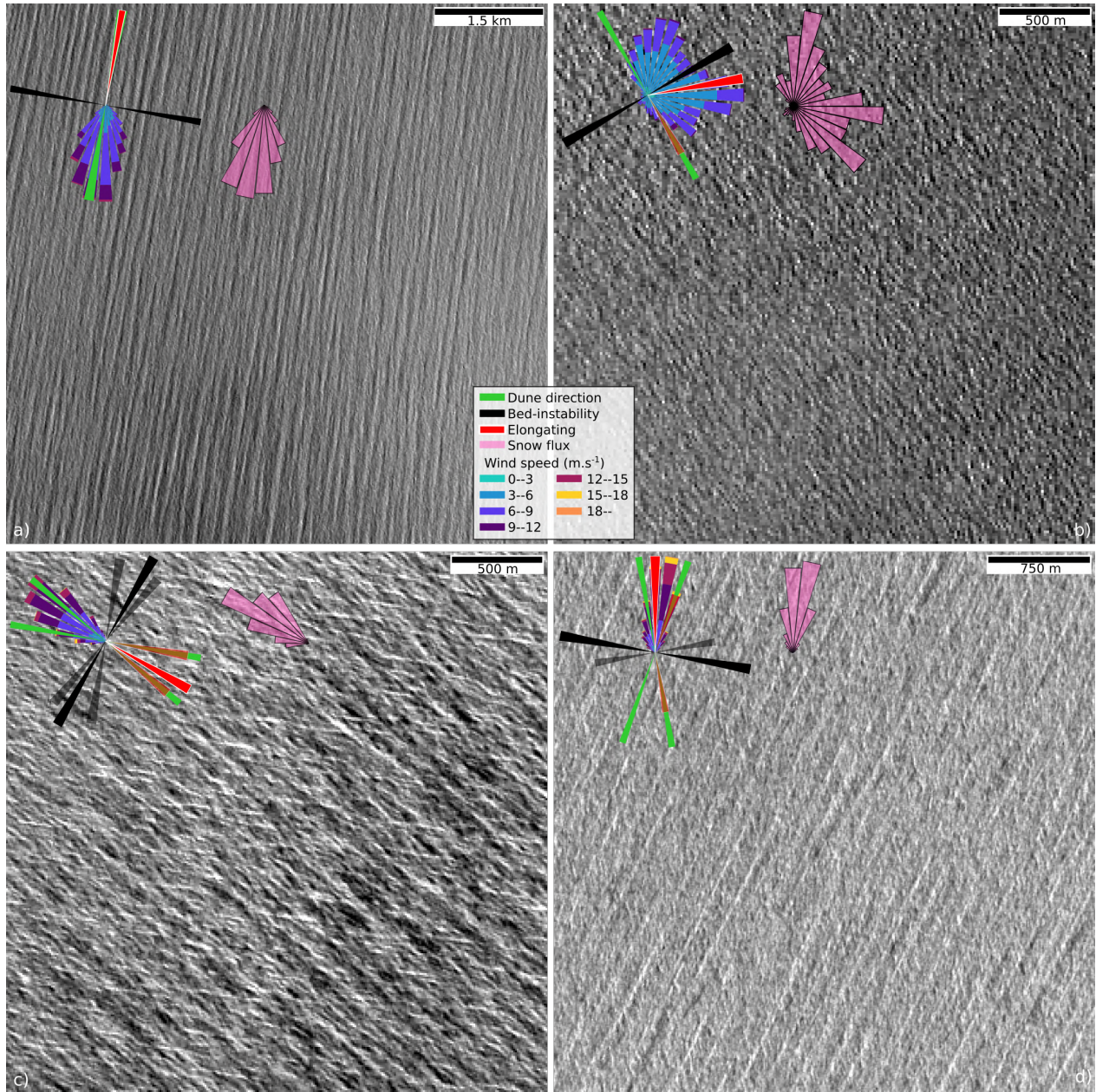


Figure 12: Sentinel-2 images (NIR channel) of (a) dunes with a single orientation (80°S, 28.75°E) (b) dunes in complex wind regime (79.75°S, 93°E), and (c) dunes with two orientations (72.25°S, 50.5°E), and (d) same as (c) (70°S, 140°E). The roses show the observed dune orientation, elongating orientation, bed-instability orientation, and snow flux (pink). Elongating and bed-instability modes calculated over 2018–2021 are shown in solid color (red and black respectively), while these modes calculated for the last precipitation event only are shown with semi-transparency (red and black respectively).

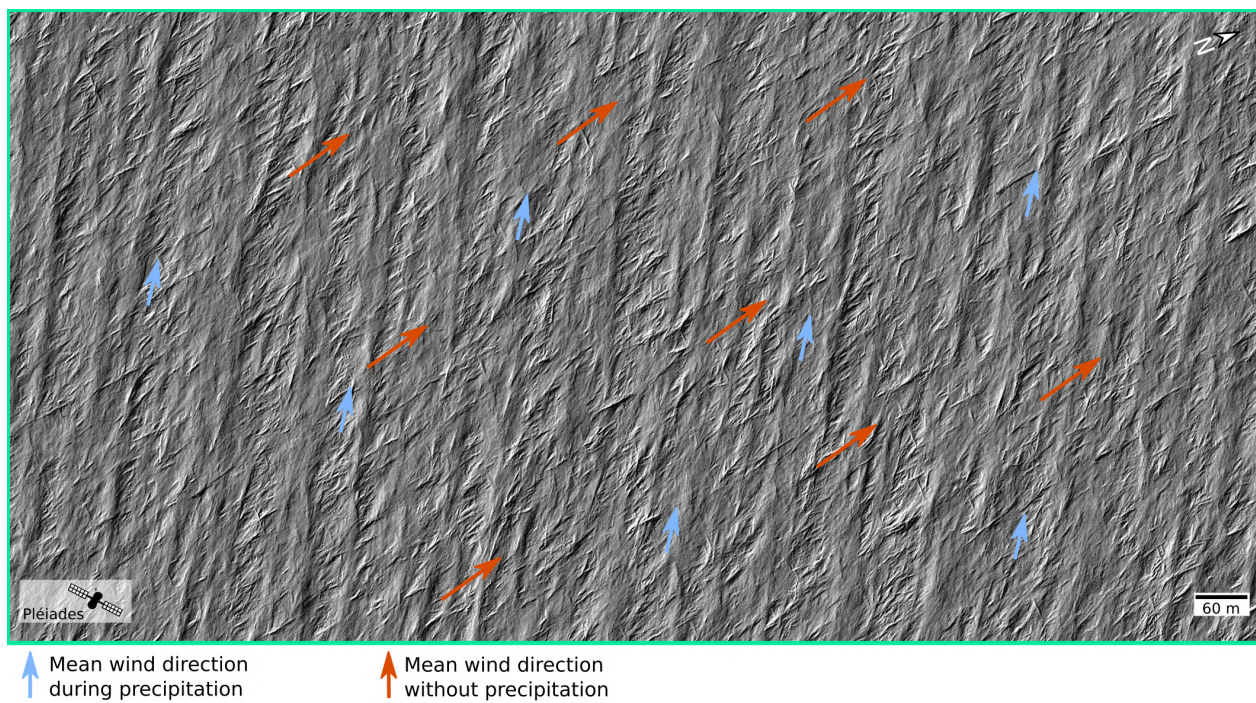


Figure 13: 75-cm resolution Pleiades image (67.47°S, 138.48°E) showing sastrugi and bigger linear dunes. The direction of the sastrugi is aligned on the wind direction with no precipitation (red arrows) and the dune direction is aligned with the wind direction during precipitations (blue arrows).

Supplementary Notes



Figure 14: Diagram synthesizing the method to retrieve dune orientations from satellite images and to calculate the elongating mode and bed-instability mode orientations from the ERA-5 reanalysis.

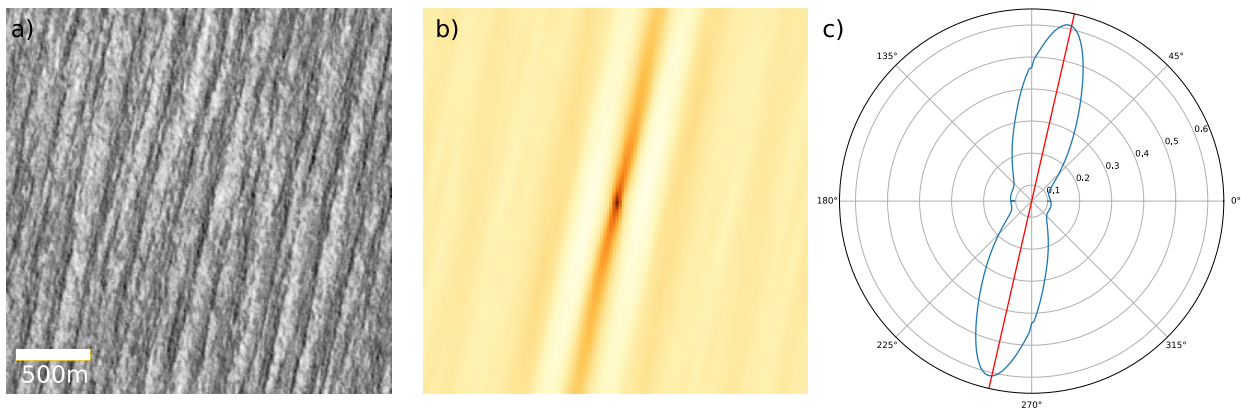


Figure 15: Illustration of dune orientation retrieval using 2D autocorrelation. (a) sub-image from Sentinel-2 with linear dunes, (b) 2D spatial autocorrelation function, and (c) radius-integrated autocorrelation function as a function of the orientation angle (blue) and detected orientation (red) corresponding to the maximum of this function.

Supplementary Text

Sentinel-2 satellite images are available from late 2015 up to present, and Landsat-8 satellite images from 2013 to present. The analysis has been conducted on satellite images acquired in November and December for 2013, 2018, 2019, 2020, 2021, and in January and February 2022. The orientations analyzed in the main text are the combined orientations estimated for early spring (over November and December) during the 4 continuous years 2018, 2019, 2020, and 2021 using the circular Kernel Density Estimation [6]. The other orientation data are used to check our hypothesis that the global patterns are mostly persistent over years and seasons.

References

- [1] Richard Bintanja, H. Lilienthal, et al. “Observations of snowdrift over Antarctic snow and blue-ice surfaces”. In: *Annals of Glaciology* 32 (2001), pp. 168–174. ISSN: 0260-3055, 1727-5644. DOI: [10.3189/172756401781819076](https://doi.org/10.3189/172756401781819076).
- [2] Benjamin Pohl, Vincent Favier, et al. “Relationship Between Weather Regimes and Atmospheric Rivers in East Antarctica”. In: *Journal of Geophysical Research: Atmospheres* 126.24 (2021), e2021JD035294. ISSN: 2169-8996. DOI: [10.1029/2021JD035294](https://doi.org/10.1029/2021JD035294).
- [3] Ernesto Trujillo, Katherine Leonard, et al. “Changes in snow distribution and surface topography following a snowstorm on Antarctic sea ice”. In: *Journal of Geophysical Research: Earth Surface* 121.11 (2016), pp. 2172–2191. ISSN: 2169-9011. DOI: [10.1002/2016JF003893](https://doi.org/10.1002/2016JF003893).
- [4] S. Courrech du Pont, C. Narteau, et al. “Two modes for dune orientation”. In: *Geology* 42.9 (Sept. 1, 2014), pp. 743–746. ISSN: 0091-7613, 1943-2682. DOI: [10.1130/G35657.1](https://doi.org/10.1130/G35657.1).
- [5] R. A. Schmidt. “Properties of blowing snow”. In: *Reviews of Geophysics* 20.1 (1982), pp. 39–44. ISSN: 1944-9208. DOI: [10.1029/RG020i001p00039](https://doi.org/10.1029/RG020i001p00039).

- [6] Charles C. Taylor. “Automatic bandwidth selection for circular density estimation”. In: *Computational Statistics & Data Analysis* 52.7 (Mar. 15, 2008), pp. 3493–3500. ISSN: 0167-9473. DOI: [10.1016/j.csda.2007.11.003](https://doi.org/10.1016/j.csda.2007.11.003).